

# A Real-Time Multi-Task Learning System for Joint Detection of Face, Facial Landmark and Head Pose

Qingtian Wu<sup>1</sup>, Member, IEEE, Xiaoming Wang<sup>1</sup>, Student Member, IEEE,

Liming Zhang<sup>1</sup>, Member, IEEE, and Fei Richard Yu<sup>1</sup>, Fellow, IEEE

**Abstract**—Extreme head postures pose a common challenge across a spectrum of facial analysis tasks, including face detection, facial landmark detection (FLD), and head pose estimation (HPE). These tasks are interdependent, where accurate FLD relies on robust face detection, and HPE is intricately associated with these key points. This paper focuses on the integration of these tasks, particularly when addressing the complexities posed by large-angle face poses. The primary contribution of this study is the proposal of a real-time multi-task detection system capable of simultaneously performing joint detection of faces, facial landmarks, and head poses. This system builds upon the widely adopted YOLOv8 detection framework. It extends the original object detection head by incorporating additional landmark regression head, enabling efficient localization of crucial facial landmarks. Furthermore, we conduct optimizations and enhancements on various modules within the original YOLOv8 framework. To validate the effectiveness and real-time performance of our proposed model, we conduct extensive experiments on 300W-LP and AFLW2000-3D datasets. The results obtained verify the capability of our model to tackle large-angle face pose challenges while delivering real-time performance across these interconnected tasks.

**Index Terms**—Multitask learning, face detection, facial landmark detection, head pose estimation, real-time system

## I. INTRODUCTION

IN recent years, the rapid advancement of deep learning techniques has revolutionized various computer vision tasks, particularly in the tasks of facial analysis tasks, including face detection, facial landmark detection (FLD), and head pose estimation (HPE). Among them, face detection is a continuously and widely discussed topic; FLD entails identifying key points on a face, such as eyes, nose, and mouth corners; HPE involves determining the orientation and position of a person's head relative to the camera or a reference frame. These tasks have witnessed substantial progress and development, making them essential in numerous applications, including human-computer interaction [1], face recognition [2], facial expression analysis [3] and driving assistance system [4], [5].

Qingtian Wu, Xiaoming Wang and Liming Zhang (Corresponding author) are with the Department of Computer and Information Science, Faculty of Sciences and Technology, University of Macau (E-mail: {yc07452, lmzhang}@um.edu.mo).

F. Richard Yu is with the Shenzhen Key Laboratory of Digital and Intelligent Technologies and Systems, Shenzhen University, Shenzhen 518060, China (e-mail: yufei@szu.edu.cn).

This work was supported in part by the Science and Technology Development Fund of Macau SAR under Grant 0060/2021/A and 0071/2022/A, and in part by the Multi-Year Research Grant under Grant MYRG2022-00193-FST.

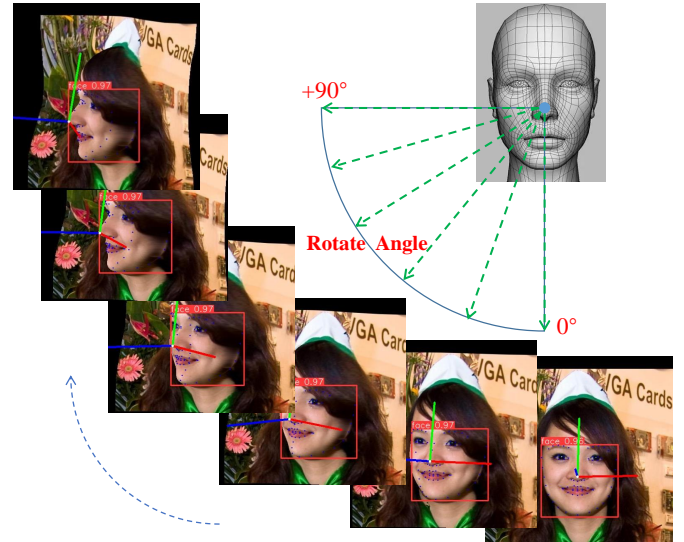


Fig. 1. Our multitask learning system can simultaneously detect faces, facial landmarks, and head posture, from front to side faces. (Best view in zoom).

However, despite the promising results achieved in each individual tasks, at least two challenges hinder their seamless integration into internet of things (IoT) applications:

- **Real-time requisites of practical systems.** For instance, this timely response plays a pivotal role in averting hazardous driving behaviors, ultimately safeguarding lives and mitigating potential accidents in assisted driving systems. However, the conventional approach [6] involves a sequential procedure: first detecting faces, followed by key point detection, and subsequently assessing fatigue status or ascertaining head posture based on these outputs. Yet, this sequential cascade not only consumes time but also exerts a substantial demand on computational resources.
- **Multitask learning in a unified framework.** Various facial analysis tasks are treated as distinct entities, trained and supervised individually. This approach stems from the fact that task learning is closely tied to specific annotation information for real samples. However, when it comes to multitask learning, the inclusion of multiple annotation sources becomes a considerably more time-intensive and labor-demanding endeavor. Moreover, from

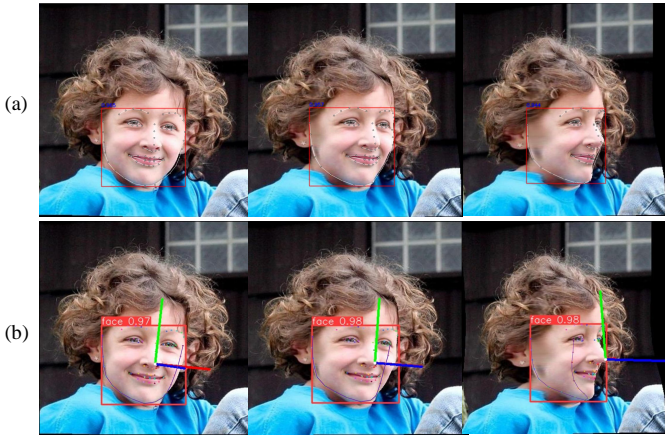


Fig. 2. Distinct approaches to modeling 2D facial landmarks. (a) 2D FLD extracted from observable contours. (b) 2D FLD acquired by projecting its corresponding 3D coordinates. (Best view in zoom).

the perspective of model development, the incorporation of supplementary modules to cater to different subtasks presents an additional challenge.

To address the above challenges, we propose the following strategies: Initially, we intend to unify face detection and FLD within a single framework, leveraging the YOLOv8 detection framework as a foundation for learning. We draw inspiration from YOLOPose’s methodology, a framework tailored for human pose estimation. By adapting the human label into face label, we expand the scope of the human body key points to encompass a wider array of facial landmarks. This approach is intricately woven into the design of our baseline model. We introduce our YOLO-based model for multitask learning, aptly named YOLOMT.

For head pose estimation, a conventional technique involves utilizing the classic PnP algorithm. This method entails comparing the estimated 2D facial keypoints with the 3D keypoints of a standardized model to derive a rotation matrix, subsequently yielding the three Euler angles that define the head pose. However, a drawback of this method is its reliance on 2D key point estimations derived from visible contours, while actual 2D key points are obtained through the projection of 3D key points. The disparity between the two can be observed in Fig. 2. To mitigate computational overhead, we forego designing additional models for direct head pose estimation. Instead, we opt for an indirect approach by estimating the 2D key points resulting from the 3D projection, thereby inferring the head pose indirectly.

To handle the scarcity of labeled data for extreme facial poses, data augmentation and transfer learning are employed in our approach. By artificially generating data with augmented poses and leveraging pre-trained models on related tasks, the model can better generalize to challenging scenarios.

To achieve real-time performance, we base our model on the lightweight version of YOLOv8 architecture to balance accuracy and efficiency. We also undertake optimal learning on certain original modules of YOLOv8, including reparameterized stem and bottleneck. We seamlessly incorporate the

reparameterization technique into traditional convolutional operations, thereby transforming the original YOLO components to possess richer feature representations while maintaining a reduced computational burden. Empirical experimentation demonstrates that enhancing these modules leads to an observable enhancement in the accuracy of FLD.

The contributions of this work are summarized as follows:

- We achieve an end-to-end approach for concurrent face detection and FLD, built upon the latest YOLOv8 framework. To improve the balance between the inference speed and detection accuracy, we adopt some cheap operations such as the reparameterization technique to modify the original YOLO components (stem and bottleneck) for accurate FLD.
- Different from other conventional 2D FLD approaches that primarily focus on identifying 2D key points derived from visible contours, we can estimate accurate 2D facial landmarks that directly correspond to their underlying 3D structures. Experimental results on the AFLW2000-3D dataset [7] demonstrate that our proposed YOLOMT can achieve top 1 accuracy of FLD with a mean normalized mean error (NME) of 3.02.
- Capitalizing on the estimated 2D facial landmarks, we achieve nearly effortless and accurate HPE by employing the PnP algorithm. Notably, the accomplishment of these three tasks necessitates the implementation of an end-to-end model. Moreover, experiments on AFLW2000-3D dataset show that our tiny YOLOMT maintains robustness and accuracy even when confronting extreme facial postures and achieving an impressive detection speed of 102 frames per second (FPS).

The rest of the paper is organized as follows. In Section II, we provide a review of related works on multitask learning including the task of face detection, FLD and HPE. Section III presents the detailed description of our proposed YOLOMT. In Section IV, we compare and analyze the experimental results of our method with other existing methods. Finally, we draw our conclusions in Section V.

## II. RELATED WORKS

### A. Multitask Learning

In the context of learning paradigms, single-task learning (STL) involves treating each attribute or task as an isolated entity. A distinct model is created for each task, disregarding any potential connections between them. Conversely, multitask learning (MTL) entails the development of a unified model to learn shared representations that simultaneously benefit multiple tasks.

Within the domain of facial-related detection tasks, such as FLD and HPE, MTL has garnered significant adoption. It offers the advantage of concurrently detecting multiple facial attributes. For example, a residual multitask learning framework is proposed in [8] to jointly achieve FLD and expression recognition simultaneously by using the complementary information between the two tasks. In [9], a MTL framework is adopted in a multi-view facial expression recognition model that regards HPE as an auxiliary task. In [10], a multitask

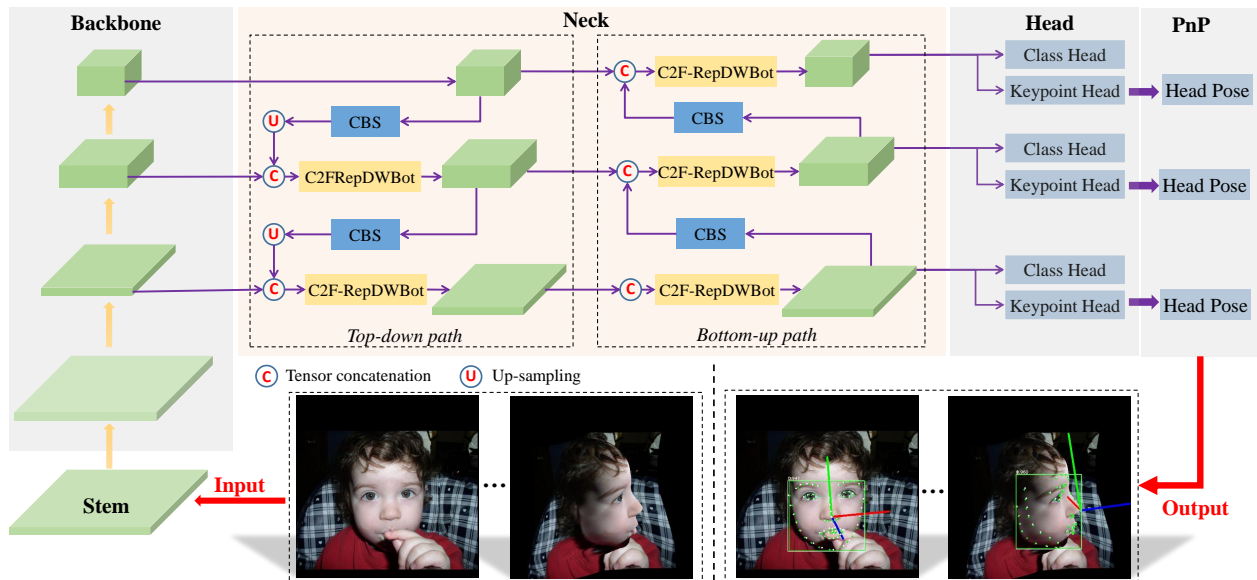


Fig. 3. The overall structure of our proposed YOLOMT. It contains five components (i.e., Stem, Backbone, Neck, Head and the PnP part). The Stem is designed to generate low-semantic feature maps, serving as input to the Backbone to generate a hierarchy of pyramid features. The Neck is designed with a bidirectional network to effectively fuse these features. The Head consists of two branches: one for face detection and the other for FLD. Subsequently, the PnP algorithm is employed to evaluate the head posture by leveraging the information obtained from the detected keypoints.

manifold method is proposed for HPE by using multimodal data. In [11], it proposes a multi-task learning algorithm by fusing the intermediate layers of deep separate CNN for simultaneous face detection, FLD, HPE and gender recognition. Our proposed YOLOMT, adapts the MTL paradigm within the YOLOv8 framework, yet with several key differentiators compared to existing strategies [9]–[12]:

- Unlike the MTL approach in [11], which primarily addresses sparse (5-point) FLD, our primary focus centers around achieving a relatively dense (68-point) FLD.
- Differing from existing methods [9], [10] that leverage auxiliary tasks to assist the primary task, we aim to enhance the overall accuracy of facial attributes by harnessing shared deep features.
- Unlike the methods in [6], [12], which adopt a two-step pipeline involving CNN features followed by attribute classifiers, our proposed YOLOMT represents an end-to-end learning approach;

### B. Facial Landmark Detection with Deep Learning

FLD is a prominent research area within computer vision, involving the precise localization of predefined landmarks on human faces. Over the years, FLD has evolved, with deep learning techniques leading to remarkable strides in accuracy and robustness. The methodologies in this field can be broadly categorized into two groups: regression-based and heatmap-based methods.

Currently, the state-of-the-art (SOTA) performance is derived from the two-stage paradigm. This approach initially captures faces using ground truth and subsequently focuses on refining networks for precise FLD. Some implementations employ high-resolution structures to generate heatmaps for accurate landmark localization, as seen in ADA [13], AWing

[14], and HRNet [15]. For instance, ADA employs attention-based networks for high-resolution facial image predictions. AWing introduces adaptive wing loss to enhance heatmap regression, while HRNet maintains high-resolution representations throughout the process for accurate keypoint estimation.

Addressing the complexity of high-resolution heatmap generation, the Pixel-in-Pixel Network (PIPNet) [16] integrates local constraints from neighboring landmarks. Popular FLD models like Convolutional Pose Machines (CPM) [17], Hour-glass Networks [18], DLIB [19], 300W [7], and MTCNN [20] have been widely utilized in various applications.

Recent trends indicate a shift towards the single-stage paradigm for FLD. In this approach, FLD is treated as an additional task during human face detection, leading to efficient detection with reduced computational demands. YOLO5Face [21], for instance, adopts an end-to-end approach for sparse (5-point) FLD, differing from our focus on dense (68-point) FLD. While RetinaFace [22] jointly detects faces and dense facial landmarks, its training remains unsupervised, and detailed information regarding its methodology is yet to be disclosed. It's worth noting that achieving end-to-end dense keypoint detection is a formidable task, grappling with challenges such as training convergence and localization accuracy concerns.

### C. Head Pose Estimation

HPE addresses the task of ascertaining the three-dimensional orientation and direction of the human head, typically captured in computer vision through Euler angles. These angles encompass rotation, pitch, and roll, collectively describing the head's spatial orientation. HPE holds significance across diverse domains, finding applications in robot vision, motion tracking, and single camera calibration. Nevertheless, it presents inherent challenges stemming from

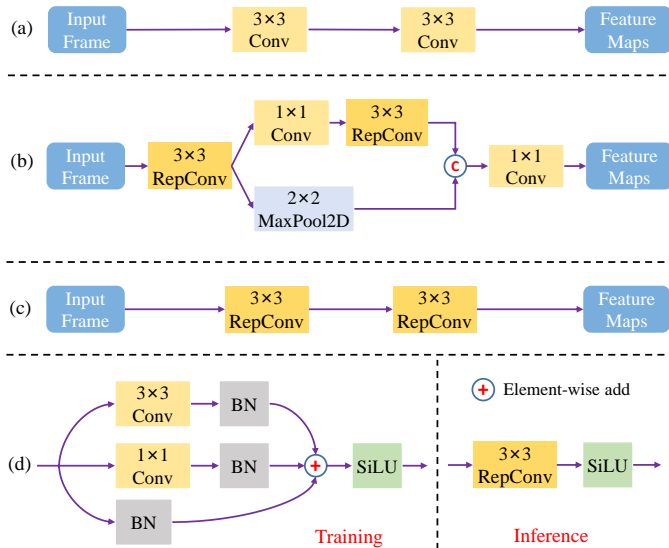


Fig. 4. Various stems. (a) The naive YOLOv8 stem. (b) The RepV7Stem. (c) The RepV8Stem. (d) Different stages in RepConv.

complex backgrounds, including extreme head postures, facial expressions, and occlusions.

Numerous methodologies have been developed to address these challenges. For instance, a matrix fisher distribution module is proposed in [23] to achieve robust head pose estimation in low pose tolerance. In [24], it introduces a lightweight model for head pose estimation from a single image, achieved through the acquisition of a fine-grained structural mapping that spatially organizes features prior to their aggregation from a single image. A nonuniform Gaussian-label network [25] is proposed for HPE under active infrared (IR) illumination. [26] presents a 3D gaze model that learns temporal information to estimate gaze uncertainty in the wild. This paper aims to achieve real-time joint detection while simultaneously estimating head posture using facial landmarks. It particularly focuses on scenarios involving extreme head postures, such as extreme head swings or elevated head angles.

### III. METHODOLOGY

In this section, we provide a comprehensive overview of our approach, YOLOMT. This methodology leverages the fundamental YOLOv8 framework and incorporates a dual-branch detection head. This enhanced architecture facilitates the concurrent detection of both faces and their detailed landmarks. By leveraging essential facial landmarks, particularly those associated with the eyes, mouth, nose, lower lips, and left and right cheeks, we utilize the Perspective-n-Point (PnP) algorithm to accurately estimate head postures. This approach remains robust even when addressing extreme orientations.

#### A. Network Architecture

The overall architecture for FLD is illustrated in Fig. 3, which contains four components (i.e., Stem, Backbone, Neck and Head).

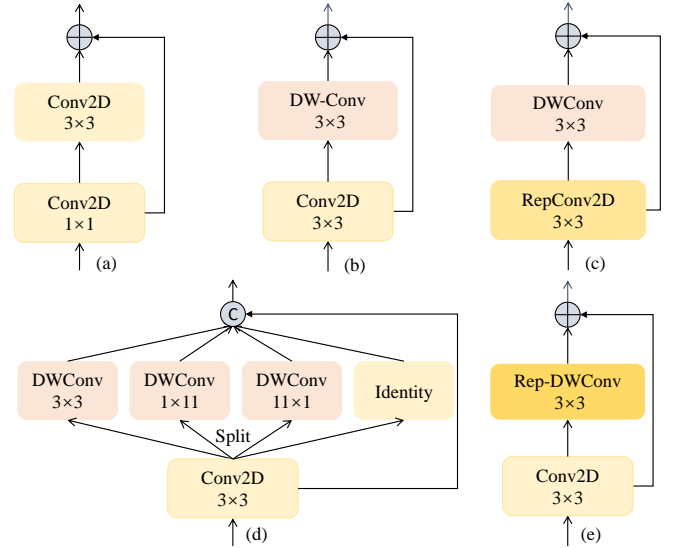


Fig. 5. Various bottlenecks. (a) The YOLOv5 bottleneck. (b) The YOLOv8 bottleneck. (c) Reparameterized YOLOv8 bottleneck with Conv2D. (d) InceptionNext bottleneck. (e) Reparameterized YOLOv8 bottleneck with DW-Conv2D.

1) **Stem**: The initial stem module takes the raw input image(s) as input and generates low-level semantic feature maps as output. We aim to devise a resource-efficient approach for this stage, one that can capture a wealth of features while keeping computational demands low.

We explore three stem structures, which are depicted in Fig. 4. The original YOLOv8 stem is illustrated in Fig. 4(a), which contains two simple convolutional operations. In Fig. 4(b), we present the Re-parameterized YOLOv7 stem, featuring two branches: a max-pooling branch, designed to reduce computational load, and a small-kernel branch ( $k = 1, 3$ ), aimed at enhancing the visual receptive fields of the features. We embrace the RepConv technique to replace the original Conv3x3. Furthermore, we apply RepConv to directly modify the YOLOv8 stems, as depicted in Fig. 4(c).

The details of RepConv are as shown in Fig. 4(d), where it capitalizes on employing small-kernel Convolutions ( $k = 0, 1, 3$ ) within a multi-branch architecture. This strategy facilitates the acquisition of intricate features during the training phase, after which the kernels are re-parameterized to form a singular 3x3 kernel during the inference phase. As a result, our approach can effectively learn diverse features with varying visual receptive fields during training, and streamline computations by consolidating multi-branches into a unified stream during inference. Both Conv and RepConv employ the Sigmoid Linear Unit (SiLU) as their activation function. We refer to the operational unit, consisting of Convolution, Batch normalization, and SiLU activation, as CBS. The ablation study of the Stem modules will be presented in Sec. IV-C within the experimental section.

2) **BottleNeck**: The backbone's fundamental unit, referred to as a bottleneck, holds a pivotal role in acquiring effective features. Inspired by the success of ResNet [27], contemporary architectures incorporate residual connections to shape the

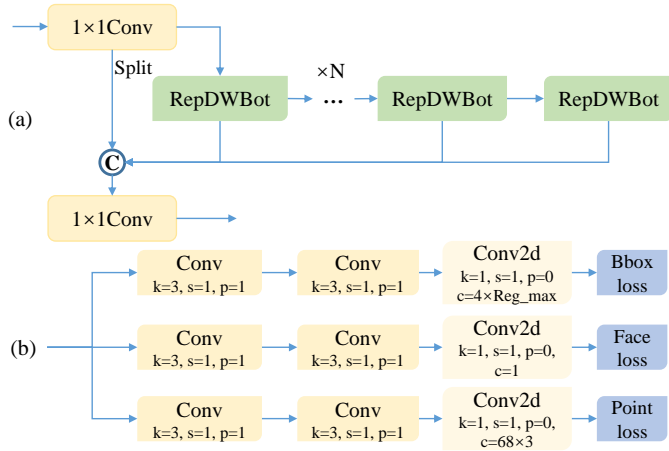


Fig. 6. Different modules. (a) C2f structure with RepDWBot. (b) Detection head with three branches: one for face BBox localization, another for face label prediction, and the third one for facial keypoint localization.

bottleneck. In the context of YOLOv5, a simplified version of the residual bottleneck, termed V5Bot, is constructed using two convolutional layers, as depicted in Fig. 5(a). Fig. 5(b) displays the YOLOv8 bottleneck (v8Bot), wherein a larger kernel size of  $3 \times 3$  is adopted in Conv and DW-Conv.

To further amplify feature representation while conserving computational resources, we not only employ reparameterization to modify v8Bot but also incorporate the bottleneck concept inspired by InceptionNext [28]. For instance, as depicted in Fig. 5(c), we utilize RepConv to replace the conventional Convolutional layer in v8Bot, resulting in the formation of Repv8Bot. In Fig. 5(e), we employ RepConv to replace the DWConv in v8Bot, leading to RepDWv8Bot. Additionally, Fig. 5(d) illustrates the detailed structure of InceptionBot.

In Sec. IV-D, we will present a comprehensive ablation study that focuses on bottleneck learning. Through this study, we provide evidence that RepV8DWBot achieves a more favorable balance between accuracy and model capacity compared to the other bottleneck configurations shown in Fig. 5.

3) **Neck**: The neck consolidates hierarchical features from the backbone, fostering interaction among diverse scales to enhance detection, particularly for multi-scale targets. Our neck module employs the naive path aggregation network (PAN) with a bidirectional structure: the top-down and bottom-up paths. This dual approach results in multiscale, feature-rich outputs through reversible processes.

We employ the proposed RepDWv8Bot to design the Cross-Stage-Partial-connections (CSP) module, a prevalent lightweight block within the YOLO framework for learning intricate gradient flow patterns. Named RepC2f due to its incorporation of two fast convolutional operations with RepDWBot, the detailed structure of RepC2f is depicted in Fig. 6(a). We can see that this design promotes a more extensive gradient flow among these cascaded bottlenecks.

4) **Head**: The detection head is designed as an adapter to generate outputs tailored to the specific target tasks. Beyond the naive detection head of YOLOv8 that regresses the face bounding-boxes (BBox) and predicts the face label, an extra

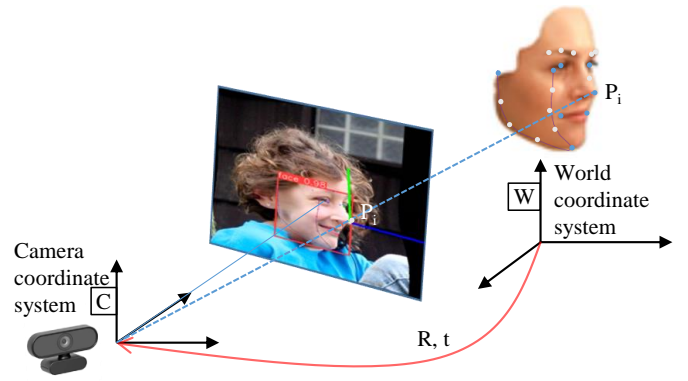


Fig. 7. The PnP algorithm.

branch is introduced to handle facial landmark regression. Fig. 6(b) shows the detection head with three branches: the face bbox branch, the face label branch and the landmark branch. Each of these branches consists of three consecutive convolutional operations, with the number of output channels in the last convolutional layer being specifically tailored to the corresponding task.

5) **PnP**: The Perspective-n-Point (PnP) problem entails determining the pose of a calibrated camera when provided with a set of  $n$  3D points in the world and their corresponding 2D projections in the image. The camera's pose encompasses 6 degrees of freedom (DOF), which consist of the rotation components (roll, pitch, and yaw) and the 3D translation of the camera concerning the world. The primary objective is to find the optimal rotation and translation values that minimize the reprojection error arising from the correspondence between 3D and 2D points.

In the process, as shown in Fig. 7, the points initially defined in the world coordinate frame  $\mathbf{X}_w$  are projected onto the image plane  $[u, v]$ . This projection adheres to the conventional perspective projection model used in cameras and is formulated as:

$$\begin{bmatrix} u \\ v \\ 1 \end{bmatrix} = \begin{bmatrix} f_x & 0 & c_x \\ 0 & f_y & c_y \\ 0 & 0 & 1 \end{bmatrix} \begin{bmatrix} 1 & 0 & 0 & 0 \\ 0 & 1 & 0 & 0 \\ 0 & 0 & 1 & 0 \end{bmatrix} \begin{bmatrix} \mathbf{R} & \mathbf{t} \\ 0 & 1 \end{bmatrix} \begin{bmatrix} X_w \\ Y_w \\ Z_w \\ 1 \end{bmatrix}, \quad (1)$$

where  $f_x$  and  $f_y$  correspond to the scaled focal lengths,  $c_x$  and  $c_y$  signify the principal point on the image plane. The variables  $\mathbf{R}, \mathbf{t}$  denote the 3D rotation and 3D translation of the camera, respectively, which are the parameters being calculated (referred to as extrinsic parameters). These values are essential for characterizing the camera's pose with respect to the world.

The Efficient PnP (EPnP) method, introduced in [29], offers a solution to the general PnP problem for cases where  $n \geq 4$ . This method operates on the premise that each of the  $n$  points (referred to as reference points) can be expressed as a weighted sum of four virtual control points. Consequently, the coordinates of these control points become the unknowns in the PnP problem, from which the final camera pose is

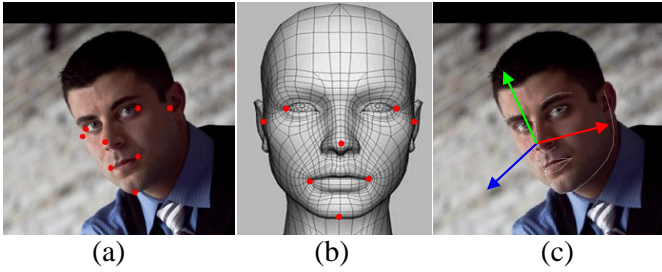


Fig. 8. Selecting specific facial keypoints to estimate the head posture by using PnP. (a)

determined. We choose 8 estimated 2D keypoints, specifically the chin, nose tip, left and right mouth corners, left and right eye corners, and left and right cheeks, as depicted in Fig. 8(a). By utilizing the EPnP algorithm to align these key points with their respective positions in the 3D model, as shown in Fig. 8(b), we can calculate the rotation matrix  $\mathbf{R}$  and the translation matrix  $\mathbf{t}$ . Fig. 8(c) shows the head posture corresponding to the rotation matrix  $\mathbf{R}$ .

### B. Face Detection

Building upon [30], a human pose estimation framework rooted in the YOLOv5 architecture, we adapt it to detect face label and their 68 key point positions instead of human label with sparse 17 keypoints. Unlike YOLOv5, YOLOv8 does not rely on predefined anchors for extracting candidate sets; it operates in an anchor-free manner. The header module in YOLOv8 undergo a transformation from the coupled structure of YOLOv5 to the decoupled structure depicted in Fig. 6(b). This modification retains the decoupled classification and regression branches. Furthermore, the regression branch has been reformulated using the integral form proposed in the distribution focus loss (DFL).

The detection head in YOLOv8 provides two types of information for each grid: the BBox location and the face confidence. The BBox location comprises four elements, namely the box center  $(C_x, C_y)$  and its width and height  $(w, h)$ . This information is compactly represented by a vector containing 5 elements, which is generated by the detection head for each grid. The vector can be expressed as:

$$O_f = (C_x, C_y, w, h, face_{conf}). \quad (2)$$

### C. Facial Landmark Detection

We extend the original YOLOPose framework, transforming the task from regressing 17 human keypoints to regressing 68 facial landmarks. In contrast to directly detecting 2D keypoints on visible contours, our approach involves detecting 2D keypoints following a 3D projection. This method possesses the distinct advantage of preserving contour information, even in scenarios involving facial movements.

Whether it pertains to a human keypoint or a facial landmark, each point information encompasses its coordinates and confidence level, denoted as  $(L_x, L_y, conf)$ . In total, the 68 facial landmarks result in 204 output elements. The landmark

head in our YOLOMT, for each anchor, produces a 204-element vector, defined as:

$$O_l = (L_x^1, L_y^1, L_{conf}^1, \dots, L_x^{68}, L_y^{68}, L_{conf}^{68}). \quad (3)$$

### D. Loss Function

For the YOLOv8 model, it utilizes the Varifocal Loss (VFL) [31] for classification and a combination of CIOU Loss [32] and Distribution Focal Loss (DFL) [33] for regression.

1) *Face classification loss*: The key enhancement in VFL is the introduction of asymmetric weighted operations, specifically tailored for positive and negative samples. This addresses the challenge of fluctuating weights caused by the imbalance between positive and negative samples, particularly crucial as accuracy calculations primarily focus on positive samples. The VFL is defined as follows:

$$VFL(p, q) = \begin{cases} -q(q \log(p) + (1-q) \log(1-p)) & q > 0 \\ -\alpha p^\gamma \log(1-p) & q = 0, \end{cases} \quad (4)$$

where  $p$  denotes the predicted IoU-aware classification score (IACS),  $q$  represents the target score. For foreground samples, their ground truth class  $q$  is set as the IoU between the generated BBox and its corresponding ground truth. Conversely, for background samples, the target  $q$  for all classes is uniformly set to 0. The scaling factors  $\alpha$  and  $\gamma$  are employed to selectively reduce the contribution of loss from negative examples ( $q=0$ ) while preserving the weight of positive examples ( $q>0$ ).

2) *Face BBox loss*: Advanced variant of IoU loss like CIOU loss has become the preferred choice in many modern object detectors for bounding box tasks. This preference originates from CIOU's scale-invariant properties and its direct optimization of the evaluation metric. In our approach, we employ the CIOU loss for bounding box supervision. For a ground truth Bbox that is associated with the grid cell  $g$  located at coordinates  $(x, y)$  and scale  $s$ , the loss can be defined as follows:

$$L_{box}(s, x, y, g) = 1 - CIOU(Box_{gt}^{s,x,y,g}, Box_{pred}^{s,x,y,g}). \quad (5)$$

Furthermore, to expedite the network's concentration on positions proximate to the target, the DFL is introduced to enhance the network's attention towards values in close proximity to the target. DFL optimizes the likelihood of positions both to the left and right of the target label, employing a cross-entropy formulation. This enables the network to swiftly converge towards a distribution centered around the genuine floating-point coordinates, with weights determined through linear interpolation from integer coordinates. This practice, referring to YOLOv8, employs DFL for rapid Bbox positioning.

3) *Face keypoint loss*: Given that both keypoint detection and object detection tasks involve localization, MS COCO [34] introduces the Object Keypoint Similarity (OKS) metric for assessing keypoint regression. OKS plays a role analogous to that of Intersection over Union (IoU) in object detection. We adhere to the definition provided by MS COCO, which is formulated as follows:

$$OKS = \sum_i [\exp(-d_i^2 / 2s^2k_i^2) \delta(v_i > \theta)] / \sum_i [\delta(v_i > \theta)], \quad (6)$$

where  $d_i$  represents the Euclidean distance between the predicted keypoint and the ground truth;  $v_i$  stands for the visibility flag associated with the ground truth keypoint;  $s$  denotes the object scale.  $k_i$  is a per-keypoint constant that governs the rate of falloff. The OKS metric ranges from 0 to 1. The keypoint loss can be defined as:

$$L_{kpts} = 1 - \sum_{n=1}^{N_{kpts}} OKS. \quad (7)$$

For each individual keypoint, we train a confidence parameter that signifies the presence or absence of that particular keypoint. In this training process, the visibility flags for keypoints are utilized as the ground truth. The keypoint confidence loss can be represented using Binary Cross-Entropy (BCE), which quantifies the loss between the predicted confidence of the  $n^{th}$  keypoint and its corresponding ground truth. This can be formulated as follows:

$$L_{kobj}(s, x, y) = \sum_{n=1}^{N_{kpts}} BCE(\delta(v_n > 0), p_{kpts}^n). \quad (8)$$

Ultimately, the total loss is computed by summing across all scales, anchors, and locations:

$$L_{total} = \sum_{s,x,y,g} (\lambda_{cls} L_{vfl} + \lambda_{box} L_{box} + \lambda_{dfl} L_{dfl} + \lambda_{kpts} L_{kpts} + \lambda_{kobj} L_{kobj}), \quad (9)$$

where  $\lambda_{cls} = 0.5$ ,  $\lambda_{box} = 7.5$ ,  $\lambda_{dfl} = 1.5$ ,  $\lambda_{kpts} = 12$ ,  $\lambda_{kobj} = 1.0$  are hyperparams chosen to balance between losses at different scales. These hyperparameter values are adopted from YOLOv8 and serve to achieve an appropriate balance among the different losses.

#### IV. EXPERIMENTS AND ANALYSIS

In this section, we provide a thorough introduction of the experimental process, including details about the datasets, the criteria used for evaluating each task, comparisons of performance with other SOTA methods.

##### A. Datasets and Evaluation Metrics

We proceed to evaluate the performance of our YOLOMT for face detection and FLD across two established benchmark datasets: 300W-LP [12] and AFLW2000 [12]. Additionally, we assess the effectiveness for HPE on AFLW2000-3D [12].

1) *300 Faces in-the-wild with large pose (300W-LP)*: Referred to as ‘‘300-W Large Pose’’, the 300W-LP dataset builds upon the original 300-W dataset [35] by synthesizing facial images that span an extensive range of head orientations, including markedly extreme poses, ranging from frontal to profile views. This amalgamation results in the 300W-LP dataset, which has become a widely adopted benchmark for tasks related to facial landmark detection and pose estimation.

We partition the dataset into two primary subsets. The training set comprises the LFPW and Helen subsets, totaling 54,232 images. In contrast, the testing set encompasses the AFW and IBug subsets, containing 6,993 images.

TABLE I  
TRAINING CONFIGURATION.

Name	Value	Name	Value
Initial learning rate	0.01	SGD momentum	0.937
Warmup momentum	0.8	Warmup epochs	3
Total training epochs	120	Weight decay	0.0005
Face Conf Threshold	0.002	IOU Threshold	0.7
Batch size	16	Image size	640×640

2) *AFLW2000-3D*: The AFLW2000-3D dataset consists of 2000 meticulously annotated images, each equipped with a comprehensive set of 68-point 3D facial landmarks at the image level. Due to its inherently demanding characteristics and the richness of its annotations, the AFLW2000-3D dataset has emerged as a dynamic benchmark for the evaluation of accuracy and robustness for FLD. It serves as a practical and pertinent testing ground for assessing the performance of deep learning models under conditions that closely emulate the intricacies of real-world scenarios.

3) *Evaluation Metrics*: Our approach encompasses the simultaneous detection of multiple tasks, including face detection, FLD and HPE. These tasks are assessed using distinct evaluation metrics. For gauging face detection accuracy, we employ the widely-used mean average precision (mAP) strategy [34] over the IoU thresholds. For evaluating the accuracy of FLD, we utilize the normalized mean error (NME) metric. This approach involves normalizing the errors by interocular distances, thus compensating for scale variations and enabling a fair comparison of results across different images. In the context of assessing the accuracy of HPE, we rely on the absolute mean error (AME) of Euler angles. Euler angles provide a concise representation of the head’s orientation in 3D space, and the AME offers a clear measurement of the deviation between the estimated and ground truth angles.

##### B. Experimental Settings

1) *Training*: As our YOLOMT framework builds upon the latest YOLOv8 detection architecture, we strive to maintain minimal modifications to the original YOLOv8 design. Consequently, our designed baseline closely adheres to the configuration of YOLOv8, encompassing training recipe including the hyperparameter settings as depicted in Table I.

The initial YOLOv8 model is pretrained on the MS COCO dataset [34]. For training our specific YOLOMT, we utilize a GPU server equipped with a GeForce 2080Ti. Each GPU has a maximum batch size of 16. We employ the SGD algorithm as our optimizer, with an initial learning rate of 1e-2. The training process is terminated at the 100-th epoch.

2) *Testing*: During the testing phase, we maintain a consistent input resolution of 640×640 pixels. In the preprocessing step, we adhere to the standard procedure utilized in the basic YOLOv5 framework. Specifically, we resize the longer side of the input frame to the desired resolution while simultaneously applying padding to the shorter side. This procedure ensures that the resulting image is square.

For assessing the inference speed of our model, we adopt a batch size of 1. This choice allows us to evaluate the real-time performance of the model, capturing its ability to process and generate predictions swiftly.

### C. Ablation Study of Stem

Based on the native YOLOv8 stem, we adopt the re-parameterization convolutions to modify the naive v8Stem to learn feature representations from cheap computational cost. Various stem modules have been introduced in Fig. 4.

We fully compare their performance on 300W-LP AFLW test set. As compared in Table II, we can see that when v8Bot is fixed as the bottleneck:

- YOLOMT with the naive v8Stem attains the highest accuracy in FLD, achieving an AP@0.5 of 82.8% and a mAP of 30.6%.
- YOLOMT with the naive v7Stem achieves 100% face detection accuracy while maintaining a minimal computational cost of 17.70G. However, the FLD performance is comparatively lower.
- YOLOMT with Repv8Stem achieves the highest face detection accuracy, both in terms of precision and recall, while preserving the same model capacity. Additionally, it achieves the highest precision and recall for FLD accuracy.

Based on the above comparative analysis, Repv8Stem is selected as the preferred stem module for YOLOMT.

### D. Ablation Study of BottleNeck

The bottleneck plays a crucial role in extracting efficient and effective features. Our objective is to design an optimal bottleneck that enhances the overall performances while preserving computational resources. We have presented various bottleneck structures in Fig. 5.

We conduct a performance comparison among these bottlenecks in Table II. From the table, we can draw the following conclusions when Repv8Stem is selected as the stem:

- YOLOMT with the naive v8Bot achieves the highest precision and a mean Average Precision (mAP) of 93.3% in face detection.
- YOLOMT with InceptionBot has the lowest number of parameters and the least computational complexity. However, its detection metrics are not increased.
- YOLOMT with Repv8DWSstem achieved the highest values in five indicators, including Recall, Precision, and AP, both in face detection and FLD, while maintaining the same model capacity.

As a result of this comprehensive evaluation, we adopt Repv8DWSstem as our preferred bottleneck.

### E. Data Augmentation

Data preprocessing have an important impact on the model performance. In our study, we investigate three combinations of data augmentation strategies. As outlined in Table III, the original  $A_0$  augmentations, including translation, scaling, flipping, and mosaics, are applied to each frame. Specifically,



Fig. 9. Different augmentation effects. (a) Using  $A_1$  to augment images. (b) Using  $A_2$  to augment images.

image translation varies within a range of  $\pm 10\%$ , scale ranges within  $\pm 50\%$ , and the probability of left-right flipping is set at 50%. Additionally, we integrate 4-image mosaics with a 100% probability.

We try to conduct comparative experiments aimed at identifying a tailored augmentation strategy that can enhance the model's capacity to handle diverse facial positions, thereby aligning with the challenges encountered in real-world detection scenarios. To achieve this, we explore two other sets of strategies denoted as  $A_1$  and  $A_2$  in Table III.  $A_1$  places a stronger emphasis on a larger scaling ratio (0.75) and incorporates mixup and copy-paste operations. On the other hand,  $A_2$  employs even more robust enhancements, featuring an even larger scaling ratio (e.g., 0.9) and the use of 9-image mosaics. The distinct effects of these image augmentation strategies are illustrated in Fig. 9.

Based on the results presented in Table IV, the following observations can be made:

- When employing the original  $A_0$  data augmentation strategy, the most favorable results are obtained across all three face detection metrics.
- The enhanced  $A_1$  data augmentation strategy, while leading to a slight reduction in face detection accuracy compared to  $A_0$ , achieves the highest accuracy in FLD.
- The most robust  $A_2$  data augmentation strategy does not yield performance improvements in either face detection or FLD.

In conclusion, the utilization of the  $A_1$  data augmentation strategy enriches detection scenarios, enhancing overall robustness and keypoint accuracy. However, it comes at the expense of a minor decrease in face detection performance.

### F. FLD Performance Comparisons with SOTAs

We conduct a comprehensive comparison with several SOTA methods, as summarized in Table V. It is important to note that the current SOTA methods primarily employ a two-stage approach to achieve high-precision keypoint detection. The "GT" notation in the table indicates that they utilize ground truth to obtain face BBoxes. Their primary evaluation metric for FLD is the Normalized Mean Error (NME).

When comparing these two-stage SOTA methods, we can observe that both SynergyNet [42] and 3DDFAv2 [6] utilize the lightweight MobileNet as their backbone network, which



TABLE II  
ABLATION STUDY OF STEMS AND BOTTLENECKS.

Stem	Bottleneck	Params(M)	Flops(G)	Face				Landmark			
				P(%)	R(%)	AP@0.5	mAP	P(%)	R(%)	AP@0.5	mAP
Naive v8Stem	v8Bot	5.08	17.71	99.9	99.7	99.5	93.1	81.8	80.9	82.8	30.6
Rep-v7Stem	v8Bot	5.08	<b>17.70</b>	<b>100.0</b>	99.6	99.5	92.9	79.7	78.5	79.1	27.8
Rep-v8Stem	v8Bot	5.08	17.71	<b>100.0</b>	99.8	99.5	<b>93.3</b>	83.8	82.8	82.0	30.1
Rep-v8Stem	InceptionBot	<b>4.61</b>	<b>16.73</b>	99.7	99.4	99.5	92.3	78.4	77.7	78.7	29.7
Rep-v8Stem	Repv8Bot	5.08	17.71	99.8	99.6	99.5	93.0	79.0	77.9	79.4	30.6
Rep-v8Stem	RepDWv8Bot	5.08	17.71	99.9	<b>100.0</b>	99.5	92.7	<b>84.9</b>	<b>84.1</b>	<b>85.2</b>	<b>31.5</b>

To expedite the process of ablation study, we employ YOLOv8-mini as the foundational model. Bold represents the best result.

TABLE III  
DIFFERENT DATA AUGMENTATIONS FOR TRAINING.

Augment	translate	scale	flip_lr	mosaic	mixup	copypaste
$A_0$	0.1	0.50	0.5	4	0.0	0.0
$A_1$	0.2	0.75	0.5	4	0.1	0.1
$A_2$	0.2	0.90	0.5	9	0.1	0.1

TABLE IV  
ABLATION STUDY OF DATA AUGMENTATION STRATEGIES.

Augment	Face			Landmark		
	P(%)	R(%)	mAP	P(%)	R(%)	mAP
$A_0$	<b>100.0</b>	<b>100.0</b>	<b>98.4</b>	98.0	97.6	69.1
$A_1$	99.8	99.7	98.3	<b>98.2</b>	<b>97.8</b>	<b>69.9</b>
$A_2$	99.7	99.8	97.7	97.9	97.5	66.4

Here, we employ YOLOv8-small as the basic model.

has the smallest model capacity (i.e., the lowest number of parameters and computational cost). Impressively, they achieve high accuracy in FLD on the AFLW2000-3D dataset, with a mean NME approaching 3.40. Furthermore, these methods demonstrate robustness even when dealing with faces rotated at large angles (i.e., between 60 and 90 degrees).

The AFLW2000-3D dataset presents a highly challenging scenario, where a limited number of images encompass more than two faces or suffer from missed detections, the potential for significant errors arises when attempting to match a detected face with its corresponding ground truth face bounding box, resulting in elevated NMEs. In line with established best practices in PRNet [40], we judiciously omit the most challenging 17 cases, where the NME exceeds 20.0. Our evaluation is therefore focused on the remaining 1983 images, which are more representative of typical scenarios.

Our end-to-end approach can achieve simultaneous detection of faces and their key points, leveraging various data augmentation techniques to enhance system robustness. A comparison in Table V reveals the following insights:

- Our YOLOMT-s outperforms other SOTA two-stage methods when using  $A_0$ ,  $A_1$  data augmentation strategies, achieving the second-lowest mean NME of 3.11 and the lowest mean NME of 3.02, respectively. This demonstrates that our end-to-end approach excels in accurately

locating the top 1 facial landmark on the dataset.

- Within the angle range of 0 to 30 degrees, both models also exhibit top-tier localization accuracy.
- In the broader ranges of 30 to 60 and 60 to 90 degrees, our approach exhibits slightly lower accuracy compared to the SOTA SynergyNet, achieving NMEs of 3.43 and 4.65, respectively. This indicates that there is potential for improvement in our method to accurately localize facial keypoints in larger range of facial oscillations.
- Our YOLOMT has a lower model capacity when using Tiny YOLOv8 as the basic framework. Compared to the small version, the parameter and computational complexity are greatly reduced, but the FLD accuracy is also slightly reduced.

### G. Robust Face Detection

The predominant approach in two-stage SOTA methods involves the dependency on GT to extract faces. This strategy offers a twofold advantage: firstly, it mitigates potential accuracy loss stemming from missed or false detections. Any such misses in the initial detection stage render the subsequent stage incapable of locating crucial facial landmarks. Secondly, this approach mitigates the additional time and computational resources required for the first stage detector. It's imperative to consider both the computational cost and time associated with the first stage detector.

However, practical applications often involve scenarios where ground truth data is unavailable. In such cases, advanced or high-speed facial detectors are typically employed in the first stage to extract facial regions. For instance, the 3DFFA method utilizes the face detector from Dlib, while 3DFFA2 adopts FaceBox [43] as its facial detection mechanism. To address this real-world scenario, we conducted empirical assessments using the AFLW2000-3D dataset.

In our study, we perform a comprehensive comparative analysis, evaluating the recognition accuracy of these two facial detectors in comparison to our end-to-end facial recognition system, as detailed in Table VI. The outcomes of our analysis indisputably highlight the superior performance of our face detectors when compared to Dlib and FaceBox. Additionally, we provide visual examples of several challenging scenarios where our detector accurately identifies faces in Fig. 10.

TABLE V  
PERFORMANCE COMPARISON WITH OTHER ADVANCED METHODS ON THE AFLW2000-3D TEST SET.

Method	Backbone	Input Size	Params (M)	Flops (G)	Face		Landmark		NME			Mean
					P(%)	mAP	P(%)	mAP	[0,30]	[30,60]	[60,90]	
Two-stage paradigm												
DenseCorr [36]	Hourglass	128×128	-	-	GT	-	-	3.62	6.06	9.56	6.41	
3DSTN [37]	VGG-16	250×250	138.36	30.84	GT	-	-	3.55	3.92	5.21	4.23	
3D-FAN [38]	Hourglass	128×128	24.00	-	GT	-	-	3.15	3.53	4.60	3.76	
3DDFA [39]	-	200×200	-	-	GT	-	-	2.84	3.57	4.96	3.79	
PRNet [40]	Hourglass	256×256	-	-	GT	-	-	2.75	3.51	4.61	3.62	
2DASL [41]	ResNet-50	120×120	23.52	8.79	GT	-	-	2.75	3.46	4.45	3.55	
3DDFAv2(MR) [6]	MobileNet	120×120	3.27	0.37	GT	-	-	2.75	3.49	4.53	3.59	
3DDFAv2(MRS) [6]	MobileNet	120×120	3.27	0.37	GT	-	-	2.63	3.42	4.48	3.51	
SynergyNet [42]	MobileNet	120×120	3.80	0.37	GT	-	-	2.65	<b>3.30</b>	<b>4.24</b>	3.41	
End-to-end paradigm												
YOLOMT-t- $A_0$	RepDWv8Bot	640×640	5.08	17.71	99.1	84.4	63.8	15.7	2.66	3.57	4.96	3.18
Our YOLOMT-s- $A_0$	RepDWv8Bot	640×640	14.02	40.70	99.3	84.9	64.8	15.9	2.57	3.52	4.87	3.11
YOLOMT-s- $A_1$	RepDWv8Bot	640×640	14.02	40.70	98.7	84.5	66.8	14.3	<b>2.51</b>	3.43	4.65	<b>3.02</b>

It should be stated that these two-stage methods use ground-truth to extract face and do not consider the computational cost in the face-detection stage. ‘-’ indicates null or not given.  $t, s$  refer to the tiny and small versions of YOLOv8.  $A_0, A_1$  represent the specific augmentation strategies.

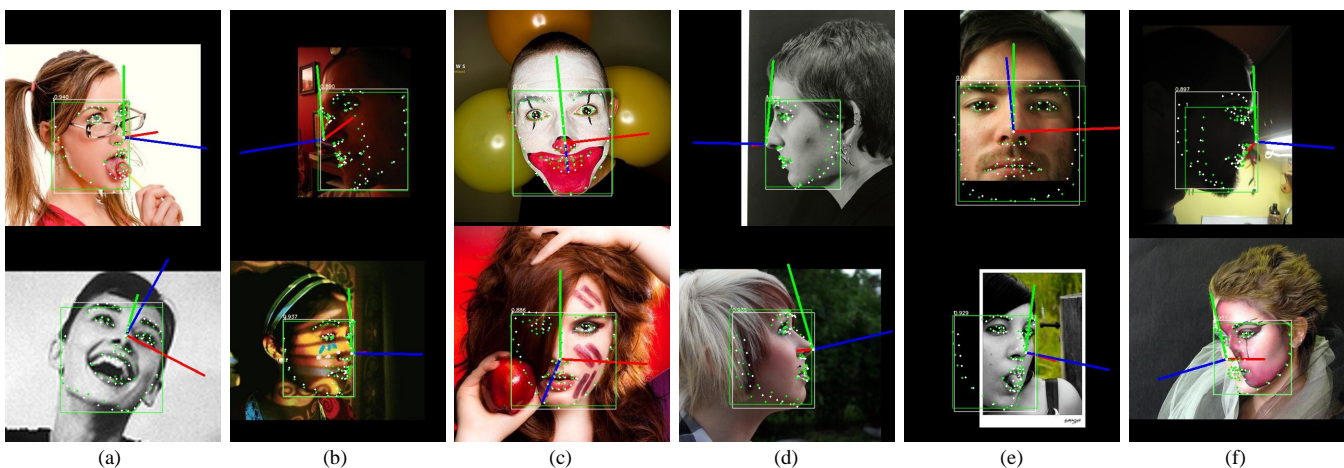


Fig. 10. More displays of three joint detection tasks under challenging conditions, i.e., (a) expressions, (b) low lighting, (c) makeups, (d) large swing angles, (e) occlusions and (f) mixed complex scenes. Green color represents ground truth and white color represents the predicted outputs. (Best view in zoom).

TABLE VI  
FACE DETECTION PERFORMANCE COMPARED WITH OTHER METHODS.

Method	DLib [19]	FaceBox [39]	Our-t	Our-s
P(%)	<80.0	98.3	99.1	99.3

Precision is calculated using AFLW2000-3D.

### H. Real-time Inference Speed

In practical applications, especially in real-time systems like facial landmark-based driver drowsiness detection, achieving high-speed performance is crucial. We conduct inference experiments on a workstation equipped with a CPU (Intel(R) Xeon(R) Gold 6134 @ 3.20GHz) and a GeForce 2080Ti GPU. The inference speed is calculated by testing validation samples

at a resolution of 640×640 with a batch size of 1.

Our proposed YOLOMT meets the real-time requirement. The time consumption of YOLOMT mainly consists of two processes: inference and non-maximum suppression (NMS), which take 9.6 and 0.6 milliseconds respectively. As a result, we achieve a real-time test speed of 98 frames per second (FPS). When utilizing the tiny YOLOMT, it achieves a speed of 102 FPS with less computational cost. Comparing the inference speed and FLD accuracy as shown in Fig. VII, we can see that:

- When our YOLOMT-s achieve the highest accuracy in FLD (i.e., with the lowest NME of 3.02), it also achieves a real-time detection speed of 102 FPS.
- Our tiny YOLOMT can further improve the inference speed to 110 FPS, but there is a slight increase in NME.
- When considering FaceBox as the face detector in this

TABLE VII  
INFERENCE SPEED COMPARISON WITH OTHER METHODS.

Method	Resolution	Params	GFlops	NME	FPS
Two-stage paradigm					
DAC-CSR [44]	100×100	-	-	6.03	10
HRNet [15]	256×256	9.70M	4.80	3.45	12
3DDFA [39]	200×200	-	-	3.79	43
3DDFAv2/FB [6]	120×120	3.27M	0.37	3.51	99
End-to-end paradigm					
Our YOLOMT-t	640×640	5.08M	17.71	3.18	<b>102</b>
Our YOLOMT-s	640×640	14.02M	40.70	<b>3.02</b>	94

two-stage system, 3DDFAv2 can detect VGA image at a speed of 99 FPS. More, this speed is achieved by cropping the face image block and resizing it to a small resolution of 120×120.

In summary, our end-to-end YOLOMT effectively balances detection accuracy and speed, providing a well-rounded solution. Fig. 10 illustrates that our YOLOMT performs well in challenging scenarios involving viewpoint variations, occlusions, changes in appearance, makeup, and multi-scale conditions, among others.

## V. CONCLUSION

In this paper, we introduce a real-time multitasking learning system named YOLOMT, built upon the YOLOv8 detection framework. YOLOMT is designed for simultaneous face detection and FLD. Furthermore, we leverage precise facial key points to estimate head posture using the PNP matching algorithm. To enhance the trade-off between speed and accuracy, we incorporate re-parameterization to modify the original YOLOv8 components (i.e., Stem and Bottleneck), resulting in an improved YOLOMT system. We empirically demonstrate the effectiveness and efficiency of YOLOMT using publicly available datasets, including 300W-LP and AFLW2000, validating its performance in real-world scenarios.

## REFERENCES

- [1] X. Liu, Y. Chen, J. Li, and A. Cangelosi, "Real-time robotic mirrored behavior of facial expressions and head motions based on lightweight networks," *IEEE Internet of Things Journal*, vol. 10, no. 2, pp. 1401–1413, 2023.
- [2] S. Yang, Y. Wen, L. He, and M. Zhou, "Sparse common feature representation for undersampled face recognition," *IEEE Internet of Things Journal*, vol. 8, no. 7, pp. 5607–5618, 2021.
- [3] G. Muhammad and M. S. Hossain, "Emotion recognition for cognitive edge computing using deep learning," *IEEE Internet of Things Journal*, vol. 8, no. 23, pp. 16894–16901, 2021.
- [4] Y. Ma, J. Wu, C. Long, and Y.-B. Lin, "Mobidiv: A privacy-aware real-time driver identity verification on mobile phone," *IEEE Internet of Things Journal*, vol. 9, no. 4, pp. 2802–2816, 2022.
- [5] J. Zhang, Y. Wu, Y. Chen, J. Wang, J. Huang, and Q. Zhang, "Ubi-fatigue: Toward ubiquitous fatigue detection via contactless sensing," *IEEE Internet of Things Journal*, vol. 9, no. 15, pp. 14 103–14 115, 2022.
- [6] J. Guo, X. Zhu, Y. Yang, F. Yang, Z. Lei, and S. Z. Li, "Towards fast, accurate and stable 3d dense face alignment," in *Proc. Euro. Conf. Comput. Vis.* Springer, 2020, pp. 152–168.

- [7] C. Sagonas, E. Antonakos, G. Tzimiropoulos, S. Zafeiriou, and M. Pantic, "300 faces in-the-wild challenge: Database and results," *Image Vis. Comput.*, vol. 47, pp. 3–18, 2016.
- [8] B. Chen, W. Guan, P. Li, N. Ikeda, K. Hirasawa, and H. Lu, "Residual multi-task learning for facial landmark localization and expression recognition," *Pattern Recognition*, vol. 115, p. 107893, 2021.
- [9] J. Chen, L. Yang, L. Tan, and R. Xu, "Orthogonal channel attention-based multi-task learning for multi-view facial expression recognition," *Pattern Recognition*, vol. 129, p. 108753, 2022.
- [10] C. Hong, J. Yu, J. Zhang, X. Jin, and K.-H. Lee, "Multimodal face-pose estimation with multitask manifold deep learning," *IEEE transactions on industrial informatics*, vol. 15, no. 7, pp. 3952–3961, 2018.
- [11] R. Ranjan, V. M. Patel, and R. Chellappa, "Hyperface: A deep multi-task learning framework for face detection, landmark localization, pose estimation, and gender recognition," *IEEE transactions on pattern analysis and machine intelligence*, vol. 41, no. 1, pp. 121–135, 2017.
- [12] X. Zhu, Z. Lei, X. Liu, H. Shi, and S. Z. Li, "Face alignment across large poses: A 3d solution," in *Proceedings of the IEEE conference on computer vision and pattern recognition*, 2016, pp. 146–155.
- [13] P. Chandran, D. Bradley, M. Gross, and T. Beeler, "Attention-driven cropping for very high resolution facial landmark detection," in *Proc. IEEE Conf. Comput. Vis. Pattern Recognit.*, 2020, pp. 5861–5870.
- [14] X. Wang, L. Bo, and L. Fuxin, "Adaptive wing loss for robust face alignment via heatmap regression," in *Proc. IEEE Int. Conf. Comput. Vis.*, 2019, pp. 6971–6981.
- [15] J. Wang, K. Sun, T. Cheng, B. Jiang, C. Deng, Y. Zhao, D. Liu, Y. Mu, M. Tan, X. Wang *et al.*, "Deep high-resolution representation learning for visual recognition," *IEEE Trans. Pattern Anal. Mach. Intell.*, 2020.
- [16] H. Jin, S. Liao, and L. Shao, "Pixel-in-pixel net: Towards efficient facial landmark detection in the wild," *Int. J. Comput. Vis.*, Sep 2021.
- [17] S.-E. Wei, V. Ramakrishna, T. Kanade, and Y. Sheikh, "Convolutional pose machines," in *Proc. IEEE Conf. Comput. Vis. Pattern Recognit.*, 2016, pp. 4724–4732.
- [18] A. Newell, K. Yang, and J. Deng, "Stacked hourglass networks for human pose estimation," in *European Conference on Computer Vision*. Springer, 2016, pp. 483–499.
- [19] D. E. King, "Dlib-ml: A machine learning toolkit," *The Journal of Machine Learning Research*, vol. 10, pp. 1755–1758, 2009.
- [20] K. Zhang, Z. Zhang, Z. Li, and Y. Qiao, "Joint face detection and alignment using multitask cascaded convolutional networks," *IEEE Signal Process. Lett.*, vol. 23, no. 10, pp. 1499–1503, 2016.
- [21] D. Qi, W. Tan, Q. Yao, and J. Liu, "Yolo5face: Why reinventing a face detector," *arXiv preprint arXiv:2105.12931*, 2021.
- [22] J. Deng, J. Guo, E. Ververas, I. Kotsia, and S. Zafeiriou, "Retinaface: Single-shot multi-level face localisation in the wild," in *Proc. IEEE Conf. Comput. Vis. Pattern Recognit.*, 2020, pp. 5203–5212.
- [23] H. Liu, S. Fang, Z. Zhang, D. Li, K. Lin, and J. Wang, "Mfdnet: Collaborative poses perception and matrix fisher distribution for head pose estimation," *IEEE Transactions on Multimedia*, vol. 24, pp. 2449–2460, 2022.
- [24] T.-Y. Yang, Y.-T. Chen, Y.-Y. Lin, and Y.-Y. Chuang, "Fsa-net: Learning fine-grained structure aggregation for head pose estimation from a single image," in *Proceedings of the IEEE/CVF Conference on Computer Vision and Pattern Recognition (CVPR)*, June 2019.
- [25] T. Liu, J. Wang, B. Yang, and X. Wang, "Ngdnet: Nonuniform gaussian-label distribution learning for infrared head pose estimation and on-task behavior understanding in the classroom," *Neurocomputing*, vol. 436, pp. 210–220, 2021.
- [26] P. Kellnhofer, A. Recasens, S. Stent, W. Matusik, and A. Torralba, "Gaze360: Physically unconstrained gaze estimation in the wild," in *Proceedings of the IEEE/CVF International Conference on Computer Vision (ICCV)*, October 2019.
- [27] K. He, X. Zhang, S. Ren, and J. Sun, "Deep residual learning for image recognition," in *Proc. IEEE Conf. Comput. Vis. Pattern Recognit.*, 2016, pp. 770–778.
- [28] Z. Liu, H. Mao, C.-Y. Wu, C. Feichtenhofer, T. Darrell, and S. Xie, "A convnet for the 2020s," in *Proceedings of the IEEE/CVF conference on computer vision and pattern recognition*, 2022, pp. 11 976–11 986.
- [29] V. Lepetit, F. Moreno-Noguer, and P. Fua, "Epnnp: An accurate o(n) solution to the pnp problem," *International journal of computer vision*, vol. 81, pp. 155–166, 2009.
- [30] D. Maji, S. Nagori, M. Mathew, and D. Poddar, "Yolo-pose: Enhancing yolo for multi person pose estimation using object keypoint similarity loss," in *Proc. IEEE Conf. Comput. Vis. Pattern Recognit.*, 2022, pp. 2637–2646.

- [31] H. Zhang, Y. Wang, F. Dayoub, and N. Sunderhauf, "Varifocalnet: An iou-aware dense object detector," in *Proceedings of the IEEE/CVF conference on computer vision and pattern recognition*, 2021, pp. 8514–8523.
- [32] Z. Zheng, P. Wang, W. Liu, J. Li, R. Ye, and D. Ren, "Distance-iou loss: Faster and better learning for bounding box regression," in *Proceedings of the AAAI conference on artificial intelligence*, vol. 34, no. 07, 2020, pp. 12 993–13 000.
- [33] X. Li, W. Wang, L. Wu, S. Chen, X. Hu, J. Li, J. Tang, and J. Yang, "Generalized focal loss: Learning qualified and distributed bounding boxes for dense object detection," *Advances in Neural Information Processing Systems*, vol. 33, pp. 21 002–21 012, 2020.
- [34] T.-Y. Lin, M. Maire, S. Belongie, J. Hays, P. Perona, D. Ramanan, P. Dollár, and C. L. Zitnick, "Microsoft coco: Common objects in context," in *Proc. Euro. Conf. Comput. Vis.* Springer, 2014, pp. 740–755.
- [35] C. Sagonas, G. Tzimiropoulos, S. Zafeiriou, and M. Pantic, "300 faces in-the-wild challenge: The first facial landmark localization challenge," in *2013 IEEE International Conference on Computer Vision Workshops*, 2013, pp. 397–403.
- [36] R. Yu, S. Saito, H. Li, D. Ceylan, and H. Li, "Learning dense facial correspondences in unconstrained images," in *Proceedings of the IEEE International Conference on Computer Vision*, 2017, pp. 4723–4732.
- [37] C. Bhagavatula, C. Zhu, K. Luu, and M. Savvides, "Faster than real-time facial alignment: A 3d spatial transformer network approach in unconstrained poses," in *Proceedings of the IEEE International Conference on Computer Vision*, 2017, pp. 3980–3989.
- [38] A. Bulat and G. Tzimiropoulos, "How far are we from solving the 2d & 3d face alignment problem?(and a dataset of 230,000 3d facial landmarks)," in *Proceedings of the IEEE international conference on computer vision*, 2017, pp. 1021–1030.
- [39] X. Zhu, X. Liu, Z. Lei, and S. Z. Li, "Face alignment in full pose range: A 3d total solution," *IEEE transactions on pattern analysis and machine intelligence*, vol. 41, no. 1, pp. 78–92, 2017.
- [40] Y. Feng, F. Wu, X. Shao, Y. Wang, and X. Zhou, "Joint 3d face reconstruction and dense alignment with position map regression network," in *Proceedings of the European conference on computer vision (ECCV)*, 2018, pp. 534–551.
- [41] X. Tu, J. Zhao, M. Xie, Z. Jiang, A. Balamurugan, Y. Luo, Y. Zhao, L. He, Z. Ma, and J. Feng, "3d face reconstruction from a single image assisted by 2d face images in the wild," *IEEE Transactions on Multimedia*, vol. 23, pp. 1160–1172, 2021.
- [42] C.-Y. Wu, Q. Xu, and U. Neumann, "Synergy between 3dmm and 3d landmarks for accurate 3d facial geometry," in *2021 International Conference on 3D Vision (3DV)*. IEEE, 2021, pp. 453–463.
- [43] S. Zhang, X. Zhu, Z. Lei, H. Shi, X. Wang, and S. Z. Li, "Faceboxes: A cpu real-time face detector with high accuracy," in *2017 IEEE International Joint Conference on Biometrics (IJCB)*. IEEE, 2017, pp. 1–9.
- [44] Z.-H. Feng, J. Kittler, W. Christmas, P. Huber, and X.-J. Wu, "Dynamic attention-controlled cascaded shape regression exploiting training data augmentation and fuzzy-set sample weighting," in *Proc. IEEE Conf. Comput. Vis. Pattern Recognit.*, 2017, pp. 2481–2490.